nature geoscience

ARTICLES

https://doi.org/10.1038/s41561-021-00730-3

Intensification of El Niño-induced atmospheric anomalies under greenhouse warming

Kaiming Hu[1,2,3] ✉, Gang Huang[1,2,4] ✉, Ping Huang[1,3], Yu Kosaka[5] and Shang-Ping Xie[6]

The El Niño/Southern Oscillation (ENSO) has a profound influence on global climate and ecosystems. Determining how the ENSO responds to greenhouse warming is a crucial issue in climate science. Despite recent progress in understanding, the responses of important ENSO characteristics, such as air temperature and atmospheric circulation, are still unknown. Here, we use a suite of global climate model projections to show that greenhouse warming drives a robust intensification of ENSO-driven variability in boreal winter tropical upper tropospheric temperature and geopotential height, tropical humidity, subtropical jets and tropical Pacific rainfall. These robust changes are primarily due to the Clausius–Clapeyron relationship, whereby saturation vapour pressure increases nearly exponentially with increasing temperature. Therefore, the vapour response to temperature variability is larger under a warmer climate. As a result, under global warming, even if the ENSO's sea surface temperature remains unchanged, the response of tropical lower tropospheric humidity to the ENSO amplifies, which in turn results in major reorganization of atmospheric temperature, circulation and rainfall. These findings provide a novel theoretical constraint for ENSO changes and reduce uncertainty in the ENSO response to greenhouse warming.

The El Niño/Southern Oscillation (ENSO) arises from complex interactions between the atmosphere and ocean[1–5]. On a timescale of 2–7 years, the eastern equatorial Pacific varies between anomalously cold (La Niña) and warm (El Niño) conditions. These swings in sea surface temperature (SST) shift atmospheric convection in the tropical Pacific and cause tropical and extratropical climate anomalies by changing the Walker circulation and exciting atmospheric teleconnection such as the Pacific–North American pattern[6–9]. Furthermore, the ENSO-induced tropical tropospheric temperature anomalies spread from the Pacific to all longitudes[10–12], broadening climate variability around the globe[12–15].

Because of the climatic effects around the globe, how the ENSO and its impacts might change in response to greenhouse warming has been investigated extensively during the past 20 years[16–24]. Coupled general circulation models (CGCMs) disagree on ENSO changes in SST due to the complexity of air–sea feedbacks in the tropical Pacific Ocean[16,25,26]. Therefore, understanding and determining how the ENSO responds to greenhouse warming remains a great challenge. A robust change in ENSO-driven rainfall variability was identified in CGCM projections[27]. Most CGCMs project an intensification of El Niño-driven drying over the western Pacific Ocean and wetting over the central and eastern equatorial Pacific[18,27–29]. Associated with changes in rainfall variability, the ENSO-forced Pacific–North American teleconnection pattern shifts eastward[30–32] and ENSO-driven precipitation variability is projected to increase in many regions around the globe[33]. However, it remains unclear how other important ENSO characteristics, such as tropospheric temperature, humidity and atmospheric circulation, might change under greenhouse warming.

Tropical humidity and temperature variability

Based on output from 19 Coupled Model Intercomparison Project Phase 6 (CMIP6) models, we examined changes in the ENSO between 1% yr^{-1} [CO_2] increase experiments and pre-industrial control experiments. We compared climate in two periods: 400–449 model years in the pre-industrial control experiments (P_{ctrl}) and 100–149 model years in the 1% yr^{-1} [CO_2] experiments (P_{warm}). From P_{ctrl} to P_{warm}, the multi-model ensemble (MME) mean of December-to-February (DJF) climatological tropical-mean (10° S–10° N) SST increased by 3.7 K, with the maximum increase located in the equatorial eastern Pacific (Fig. 1a), in agreement with previous studies[34,35]. Figure 1b compares the standard deviations of the DJF Niño3.4 SST index between two periods in each model and the MME. Hereafter, the linear trends in Niño3.4 SST index, specific humidity, air temperature, wind and geopotential height have been removed to isolate interannual variability. A different method[36] to detrend the data produced almost the same results (Extended Data Fig. 1). Among the 19 models, 11 showed an increase while the other eight showed a decrease in the standard deviation of the Niño3.4 SST index from P_{ctrl} to P_{warm}, highlighting a lack of consensus in the projection of SST variability, consistent with previous studies[16]. Nevertheless, the ENSO-driven variability in DJF tropical-mean (10° S–10° N) surface air specific humidity (q'_{sfc}) showed a coherent increase in every model (Fig. 1c). Here, the prime denotes the regression coefficient against the DJF Niño3.4 SST index, representing anomalies in tropospheric specific humidity, air temperature, geopotential height and zonal wind shown afterward. The MME q'_{sfc} increased by 33 ± 19% from P_{ctrl} to P_{warm} (hereafter, the numbers indicate the MME mean ± one standard deviation range), which is equivalent to 8.9 ± 5.1% amplification per 1-K background warming in the tropics. The regression of DJF tropical-mean (10° S–10° N) 200-hPa temperature against the Niño3.4 SST index also increased robustly in every model from P_{ctrl} to P_{warm} (Fig. 1d), by as much as 49.6 ± 32.8% (or 13.4 ± 8.8% per 1-K background tropical warming), highlighting the dramatic strengthening of the upper

[1]State key Laboratory of Numerical Modeling for Atmospheric Sciences and Geophysical Fluid Dynamics, Institute of Atmospheric Physics, Chinese Academy of Sciences, Beijing, China. [2]Laboratory for Regional Oceanography and Numerical Modeling, Qingdao National Laboratory for Marine Science and Technology, Qingdao, China. [3]Center for Monsoon System Research, Institute of Atmospheric Physics, Chinese Academy of Sciences, Beijing, China. [4]University of Chinese Academy of Sciences, Beijing, China. [5]Research Center for Advanced Science and Technology, University of Tokyo, Tokyo, Japan. [6]Scripps Institution of Oceanography, University of California, San Diego, La Jolla, CA, USA. ✉e-mail: hkm@mail.iap.ac.cn; hg@mail.iap.ac.cn

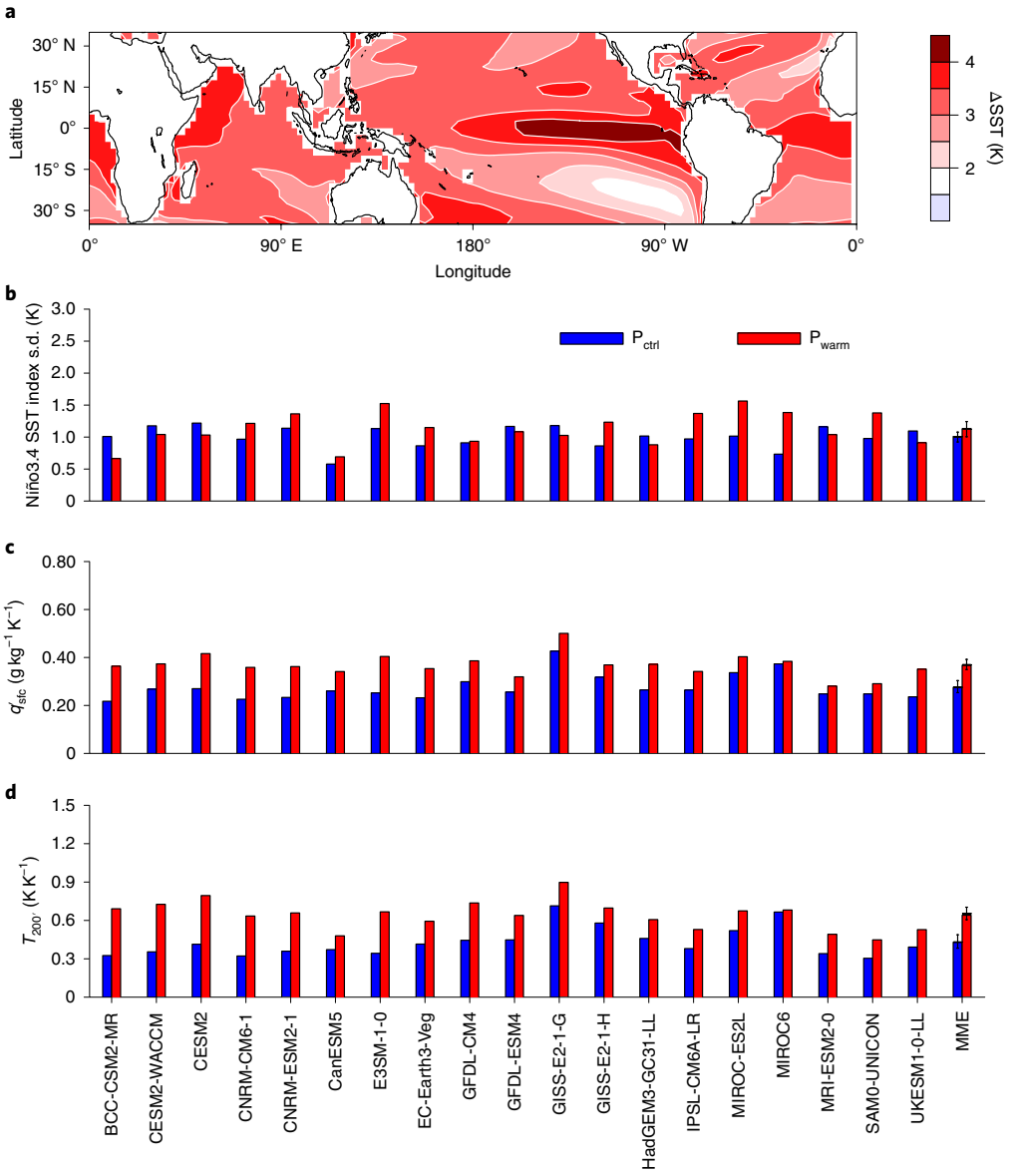

Fig. 1 | Projected changes of ENSO humidity and air temperature. a, Changes in MME mean boreal winter (DJF) climatological SST from P_{ctrl} to P_{warm}. **b**, Comparison of the standard deviation of the DJF Niño3.4 SST index over P_{ctrl} (blue) and P_{warm} (red) in each model and the MME. **c**,**d**, Comparison of DJF tropical-mean (10° S–10° N) ENSO-driven surface specific humidity (q'_{sfc}; **c**) and 200-hPa air temperature (T_{200}'; **d**) between P_{ctrl} (blue) and P_{warm} (red). Error bars in the MME mean correspond to the 95% confidence interval (see Methods).

tropospheric temperature response to the ENSO under greenhouse warming. The amplification of ENSO-driven variability in surface specific humidity and upper tropospheric temperature in the tropics was also robust across models in other scenario simulations for both CMIP5 and CMIP6 (Extended Data Figs. 2 and 3).

Why does ENSO variability amplify in tropical air humidity and tropospheric temperature under global warming? We start from the Clausius–Clapeyron expression for the saturation vapour pressure: $dq_s/dT = q_s/L(R_vT^2)$, where L is the latent heat of vaporization, R_v is the gas constant, q_s is the saturation vapour pressure and T is the air temperature. The relationship between q_s and T is nearly exponential and the value of dq_s/dT is approximately proportional to q_s[37,38]. Under global warming, q_s increases by ~7% for each 1-K increase in temperature[39], as does dq_s/dT. Since the tropical atmosphere tends to maintain a fixed tropospheric relative humidity as it warms[39], the increase of dq_s/dT means a strengthening response of vapour to air temperature variability. Thus, we can deduce that the ENSO drives a larger tropical lower tropospheric moisture anomaly in a warmer world, even if the SST variability remains unchanged.

CGCM projections agree well with the theoretical deduction. Figure 2a shows the percentage changes of DJF tropical-mean (10° S–10° N) surface dq_s/dT against the DJF tropical-mean surface air temperature increase ($\Delta\bar{T}$) in each model and the MME mean. The value of dq_s/dT was calculated as the regression of surface saturation vapour pressure against surface air temperature in each of the four periods (400–449 model years in the pre-industrial control runs and 0–49, 50–99 and 100–149 model years in the 1% yr^{-1} [CO_2] runs), which represent the reference and the three different warming stages. The linear fit has a slope of ~6.2% K^{-1}, which agrees well with the Clausius–Clapeyron scaling. The change in the response of DJF tropical surface specific humidity to air temperature (dq/dT) also generally obeys the Clausius–Clapeyron scaling, at a rate of

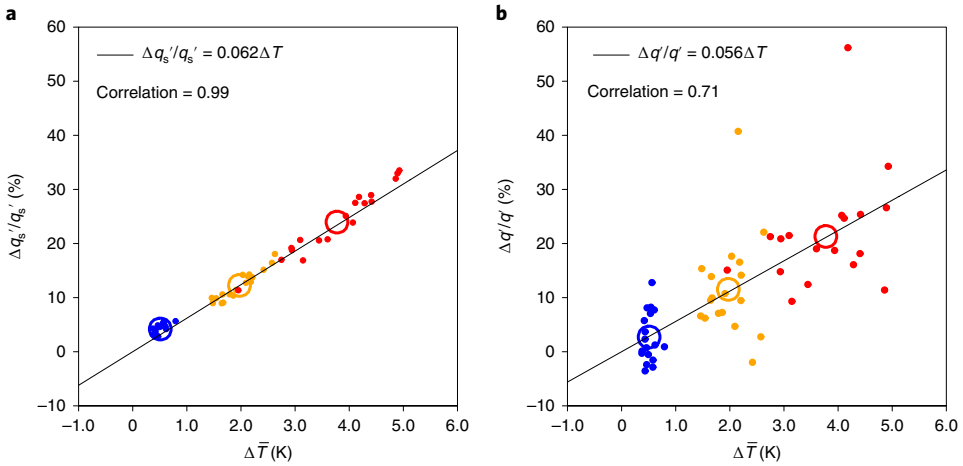

Fig. 2 | Projected changes in the tropical humidity response to air temperature under global warming. a, Percentage changes in DJF tropical-mean dq_s/dT (abbreviated as q_s') against the increase of tropical climatological surface temperature ($\Delta\overline{T}$) in each model (dots) and the MME (open circles) during three periods. The blue, orange and red colours denote the changes in the periods 0–49, 50–99 and 100–149 model years, respectively, in the 1% yr^{-1} [CO_2] runs from P_{ctrl}. The value of dq_s/dT was calculated as the regression of surface saturation vapour pressure onto surface air temperature in each period. **b**, As in **a**, but for surface-specific humidity.

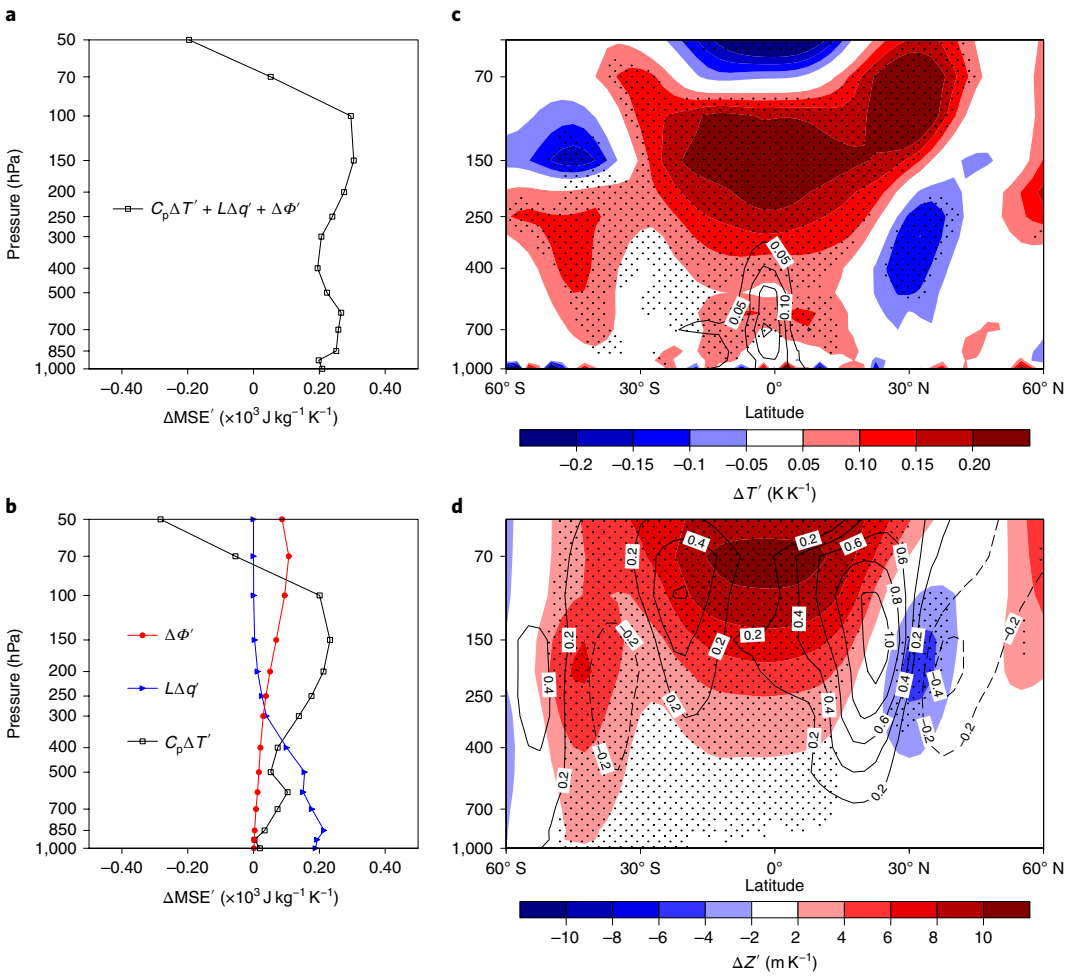

Fig. 3 | Vertical structure of the changes in ENSO humidity, temperature and circulation. a, Changes in DJF tropical-mean ENSO-driven moist static energy anomalies (ΔMSE′) in the MME. **b**, Components of the changes in moist static energy anomalies ($C_p\Delta T'$, $L\Delta q'$ and $\Delta\phi'$). **c**, Changes in DJF zonal-mean ENSO-driven specific humidity anomalies ($\Delta q'$; contours; at intervals of 0.05 g kg^{-1} K^{-1}) and air temperature anomalies ($\Delta T'$; colours). **d**, Changes in DJF zonal-mean ENSO-driven zonal wind anomalies ($\Delta U'$; black contours; at intervals of 0.2 m s^{-1} K^{-1}) and geopotential height anomalies ($\Delta Z'$; colours). In **c** and **d**, stippling indicates that more than 85% of models agree on the sign of the MME.

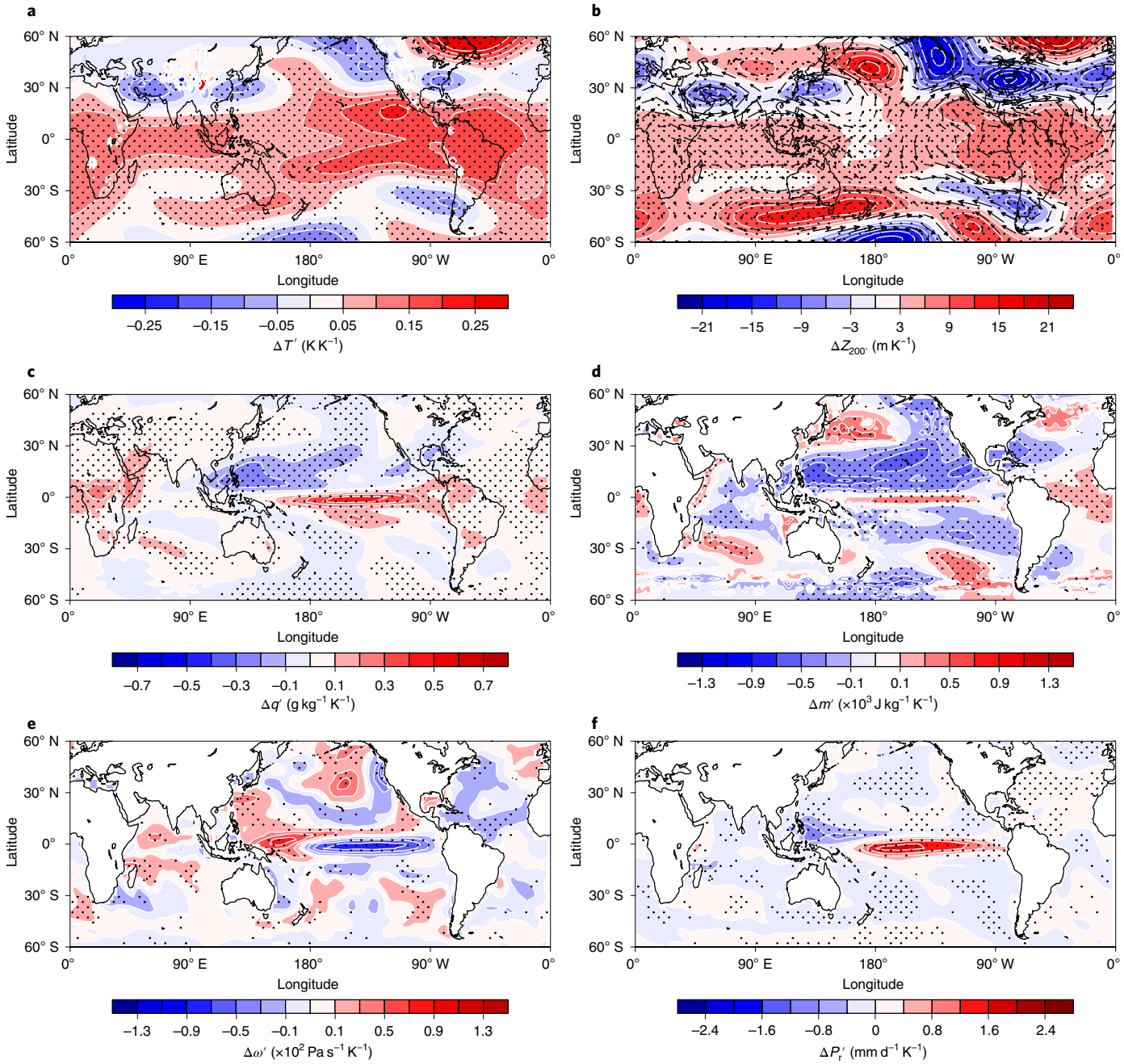

Fig. 4 | Mechanism for the changes in ENSO atmospheric circulation and precipitation. a, Changes in the ENSO-driven DJF vertically averaged (850–200 hPa) air temperature anomaly ($\Delta T'$). **b**, Changes in ENSO-driven DJF 200-hPa geopotential height ($\Delta Z_{200}'$; colours) and wind ($\Delta UV_{200}'$; vectors; arrows represent 3 m s^{-1} K^{-1}) anomalies. *UV*, zonal (*U*) and meridional (*V*) components of wind. **c**, Changes in ENSO-driven DJF low-level averaged (1,000–500 hPa) specific humidity anomalies ($\Delta q'$). **d**, Changes in ENSO-related DJF moist instability anomalies ($\Delta m'$). **e**, Changes in ENSO-driven DJF 500-hPa vertical pressure velocity anomalies ($\Delta\omega'$). **f**, Changes in ENSO-driven DJF rainfall anomalies ($\Delta P_r'$). Stippling indicates that more than 85% of models agree on the sign of the MME.

~5.6% per 1-K background warming (Fig. 2b). Compared with dq_s/dT, the relationship between dq/dT and $\Delta\bar{T}$ has some diversity, probably caused by uncertainty in the relative humidity change. Figure 3a shows the vertical profile of the change in El Niño-induced tropical-mean (10° S–10° N) moist static energy (MSE)[40] (see Methods) anomalies from P_{ctrl} to P_{warm} in the MME. In the troposphere, the El Niño-induced MSE anomaly increases almost uniformly in the vertical profile under global warming, due to moist adiabatic adjustment in convection[11,39]. Unlike MSE itself, the three components (see Methods) in the troposphere do not distribute uniformly in the vertical profile (Fig. 3b). The ENSO-induced humidity anomaly amplifies under global warming, obeying the Clausius–Clapeyron scaling, which is confined to the lower troposphere. To maintain moist adiabats in the tropics, ENSO-induced upper tropospheric temperature anomalies increase proportionally (Fig. 3b). Thus, the Clausius–Clapeyron-based mechanism can explain why ENSO-driven variability will amplify in tropical air humidity and at tropospheric temperature under global warming.

Atmospheric circulation variability

The enhanced response of tropical air temperature and humidity to the ENSO can result in a major reorganization of the atmospheric circulation. As shown in Fig. 3c, the change of zonal-mean specific humidity anomalies from P_{ctrl} to P_{warm} is mainly confined in the lower troposphere below 500 hPa, while the change of air temperature anomalies peaks at around 150 hPa. By hydrostatic balance, the El Niño-induced geopotential height anomaly strengthens in the upper tropical troposphere, with intensified westerly wind anomalies in the upper troposphere around 20° S and 20° N (Fig. 3d). Previous studies[12,15] showed that subtropical jets in both hemispheres strengthen on their equatorward flanks in El Niño events (Extended Data Fig. 4) and our results indicate that this response will amplify under global warming. We found that the El Niño-induced zonal-mean westerly wind anomalies in the upper troposphere around 20° N increase by ~61.7 ± 60% from P_{ctrl} to P_{warm}, or by 16.6 ± 16.2% for each 1-K background warming in the tropics.

Because of equatorial wave adjustments[13,37], the increase of ENSO-induced air temperature anomalies in the free troposphere spread horizontally in the entire tropics (Fig. 4a). Consequently, there are positive changes of El Niño-induced 200-hPa height anomalies within the tropics between 20° S and 20° N, and enhanced westerly wind anomalies along 20° S and 20° N due to the equatorward pressure gradient (Fig. 4b). Poleward of the tropical warming, there is a latitude belt of marked tropospheric cooling in the Northern Hemisphere, probably caused by the changes in the eddy-driven meridional circulation[12]. The cooling is prominent over the Asian continent and North America, which corresponds to robust 200-hPa low-pressure anomalies in these regions. Thus, the pressure gradient south of these regions is stronger than in other regions, and so are the westerly wind anomalies. Compared with the ENSO-induced air temperature and atmospheric circulation anomalies in the present real climate (Extended Data Fig. 5), the anomalies intensify in a warmer climate. Particularly, the westerly wind anomalies over subtropical North America (15° N–30° N, 130° W–30° W) increase from 1.9 ± 0.7 m s^{-1} K^{-1} for P_{ctrl} to 3.3 ± 0.5 m s^{-1} K^{-1} for P_{warm}, corresponding to a 19.2 ± 11.3% increase for each 1-K background tropical warming. This intensified circulation response makes the US west coast more susceptible to ENSO varibility[30–33].

Precipitation variability

The changes in ENSO-driven humidity anomalies are localized. In El Niño, SST and low-level tropospheric air temperature anomalies are positive in the tropical central-eastern Pacific but negative in the tropical Northwest Pacific. Hence, the background greenhouse warming will strengthen both the positive humidity anomalies over the central-eastern Pacific and negative humidity anomalies over the Northwest Pacific (Fig. 4c and Extended Data Fig. 6). The changes of ENSO-related gross moist instability[40] (see Methods) are primarily determined by the changes of ENSO-driven humidity anomalies, with increasing trends over the tropical central-eastern Pacific but decreasing trends in the Northwest Pacific (Fig. 4d). In the tropics, the increase of gross moist instability tends to lead to low-level convergence, and vice versa[40]. Indeed, the changes of ENSO-induced 500-hPa vertical velocity anomalies are spatially consistent with the change of gross moist instability in the tropics, with upwelling change over the equatorial central-eastern Pacific but downwelling change over the Northwest Pacific (Fig. 4e). Therefore, the enhanced response of humidity to air temperature can intensify both the El Niño-driven precipitation decrease over the Northwest Pacific and the increase over the central-eastern equatorial Pacific (Fig. 4f and Extended Data Fig. 6). This explanation does not require spatial variations in mean warming[18,27,29] or ENSO SST anomalies[41]. The relative contributions from the SST pattern effect need to be evaluated in future studies.

Year-to-year ENSO variability is controlled by complicated air–sea feedbacks and affected by the noise arising from internal variability. It proves difficult to determine how ENSO behaviours change under global warming[16,42–46]. Here, we find that the nonlinear response of saturation vapour pressure to temperature change (that is, the Clausius–Clapeyron relationship) causes robust changes in key characteristics of the ENSO under global warming. Specifically, the boreal winter response of tropical humidity, tropospheric upper temperature, the subtropical jet in both hemispheres and tropical Pacific rainfall to the ENSO intensify robustly across the models. As extreme weather often results from ENSO-induced anomalous atmospheric circulation and temperature[47–49], the intensification of ENSO-driven atmospheric variability offers a key step to project how ENSO-related extreme weather will change in the future, which deserves further studies.

This study shows that the Clausius–Clapeyron-based mechanism is an important constraint for ENSO projections. This mechanism is based on the change in the sensitivity of vapour response to temperature but not on the change in the mean-state vapour, as has been widely used in previous studies[39,50]. The response of tropospheric humidity to SST variability also intensifies elsewhere (for example, the tropical Indian Ocean and Atlantic; Extended Data Figs. 7 and 8) under greenhouse warming, suggesting that our method can be applied to projecting changes in other tropical modes.

Online content

Any methods, additional references, Nature Research reporting summaries, source data, extended data, supplementary information, acknowledgements, peer review information; details of author contributions and competing interests; and statements of data and code availability are available at https://doi.org/10.1038/s41561-021-00730-3.

Received: 29 June 2020; Accepted: 12 March 2021;
Published online: 15 April 2021

References

1. Jin, F.-F. Tropical ocean–atmosphere interaction, the Pacific Cold Tongue, and the El Niño–Southern Oscillation. *Science* **274**, 76–78 (1996).
2. Wallace, J. M. et al. The structure and evolution of ENSO-related climate variability in the tropical Pacific: lessons from TOGA. *J. Geophys. Res.* **103**, 14241–14259 (1998).
3. Neelin, J. D. et al. ENSO theory. *J. Geophys. Res.* **103**, 14261–14290 (1998).
4. McPhaden, M. J., Zebiak, S. E. & Glantz, M. H. ENSO as an integrating concept in Earth science. *Science* **314**, 1740–1745 (2006).
5. Deser, C., Alexander, M. A., Xie, S. P. & Phillips, A. S. Sea surface temperature variability: patterns and mechanisms. *Ann. Rev. Mar. Sci.* **2**, 115–143 (2010).
6. Horel, J. D. & Wallace, J. M. Planetary-scale atmospheric phenomena associated with the Southern Oscillation. *Mon. Weather Rev.* **109**, 813–829 (1981).
7. Trenberth, K. E. et al. Progress during TOGA in understanding and modeling global teleconnections associated with tropical sea surface temperatures. *J. Geophys. Res.* **103**, 14291–14324 (1998).
8. Gill, A. E. Some simple solutions for heat-induced tropical circulation. *Q. J. R. Meteorol. Soc.* **106**, 447–462 (1980).
9. Wang, B., Wu, R. G. & Fu, X. H. Pacific–East Asian teleconnection: how does ENSO affect East Asian climate? *J. Clim.* **13**, 1517–1536 (2000).
10. Chiang, J. C. H. & Sobel, A. H. Tropical tropospheric temperature variations caused by ENSO and their influence on the remote tropical climate. *J. Clim.* **15**, 2616–2631 (2002).
11. Su, H., Neelin, J. D. & Meyerson, J. E. Sensitivity of tropical tropospheric temperature to sea surface temperature forcing. *J. Clim.* **16**, 1283–1301 (2003).
12. Seager, R., Harnik, N. I., Kushnir, Y., Robinson, W. A. & Miller, J. Mechanisms of hemispherically symmetric climate variability. *J. Clim.* **16**, 2960–2978 (2003).
13. Neelin, J. D. & Su, H. Moist teleconnection mechanisms for the tropical South American and Atlantic sector. *J. Clim.* **18**, 3928–3950 (2005).
14. Xie, S.-P. et al. Indian ocean capacitor effect on Indo-Western Pacific climate during the summer following El Niño. *J. Clim.* **22**, 730–747 (2009).

15. Adames, Á. F. & Wallace, J. M. On the tropical atmospheric signature of El Niño. *J. Atmos. Sci.* **74**, 1923–1939 (2017).
16. Collins, M. et al. The impact of global warming on the tropical Pacific Ocean and El Niño. *Nat. Geosci.* **3**, 391–397 (2010).
17. Cai, W. J. et al. Increasing frequency of extreme El Niño events due to greenhouse warming. *Nat. Clim. Change* **4**, 111–116 (2014).
18. Cai, W. J. et al. ENSO and greenhouse warming. *Nat. Clim. Change* **5**, 849–859 (2015).
19. Cai, W. J. et al. Increased variability of eastern Pacific El Niño under greenhouse warming. *Nature* **564**, 201–206 (2018).
20. Yeh, S. W. et al. El Niño in a changing climate. *Nature* **461**, 511–514 (2009).
21. Yeh, S. W. et al. ENSO atmospheric teleconnections and their response to greenhouse gas forcing. *Rev. Geophys.* **56**, 185–206 (2018).
22. Fasullo, J. T., Otto-Bliesner, B. L. & Stevenson, S. ENSO's changing influence on temperature, precipitation, and wildfire in a warming climate. *Geophys. Res. Lett.* **45**, 9216–9225 (2018).
23. Perry, S. J., McGregor, S., Sen Gupta, A., England, M. H. & Maher, N. Projected late 21st century changes to the regional impacts of the El Niño–Southern Oscillation. *Clim. Dynam.* **54**, 395–412 (2020).
24. Wang, B. et al. Historical change of El Niño properties sheds light on future changes of extreme El Niño. *Proc. Natl Acad. Sci. USA* **116**, 22512–22517 (2019).
25. Watanabe, M. et al. Uncertainty in the ENSO amplitude change from the past to the future. *Geophys. Res. Lett.* **39**, L20703 (2012).
26. Kim, S. T. et al. Response of El Niño sea surface temperature variability to greenhouse warming. *Nat. Clim. Change* **4**, 786–790 (2014).
27. Power, S., Delage, F., Chung, C., Kociuba, G. & Keay, K. Robust twenty-first-century projections of El Niño and related precipitation variability. *Nature* **502**, 541–545 (2013).
28. Chung, C. T. Y., Power, S. B., Arblaster, J. M., Rashid, H. A. & Roff, G. L. Nonlinear precipitation response to El Niño and global warming in the Indo-Pacific. *Clim. Dynam.* **42**, 1837–1856 (2014).
29. Huang, P. & Xie, S. P. Mechanisms of change in ENSO-induced tropical Pacific rainfall variability in a warming climate. *Nat. Geosci.* **8**, 922–927 (2015).
30. Meehl, G. A. & Teng, H. Multi-model changes in El Niño teleconnections over North America in a future warmer climate. *Clim. Dynam.* **29**, 779–790 (2007).
31. Kug, J.-S., An, S.-I., Ham, Y.-G. & Kang, I.-S. Changes in El Niño and La Niña teleconnections over North Pacific–America in the global warming simulations. *Theor. Appl. Climatol.* **100**, 275–282 (2010).
32. Zhou, Z., Xie, S., Zheng, X., Liu, Q. & Wang, H. Global warming-induced changes in El Niño teleconnections over the North Pacific and North America. *J. Clim.* **27**, 9050–9064 (2014).
33. Power, S. B. & Delage, F. P. D. El Niño–Southern Oscillation and associated climatic conditions around the world during the latter half of the twenty-first century. *J. Clim.* **31**, 6189–6207 (2018).
34. McPhaden, M. J., Lee, T. & McClurg, D. El Niño and its relationship to changing background conditions in the tropical Pacific Ocean. *Geophys. Res. Lett.* **38**, L15709 (2011).
35. Ying, J., Huang, P., Lian, T. & Chen, D. K. Intermodel uncertainty in the change of ENSO's amplitude under global warming: role of the response of atmospheric circulation to SST anomalies. *J. Clim.* **32**, 369–383 (2019).
36. Frankcombe, L. M., England, M. H., Mann, M. E. & Steinman, B. A. Separating internal variability from the externally forced climate response. *J. Clim.* **28**, 8184–8202 (2015).
37. Xie, S. P. et al. Global warming pattern formation: sea surface temperature and rainfall. *J. Clim.* **23**, 966–986 (2010).
38. Hu, K. et al. Interdecadal variations in ENSO influences on Northwest Pacific–East Asian early summertime climate simulated in CMIP5 models. *J. Clim.* **27**, 5982–5998 (2014).
39. Held, I. M. & Soden, B. J. Robust responses of the hydrological cycle to global warming. *J. Clim.* **19**, 5686–5699 (2006).
40. Neelin, J. D. & Held, I. M. Modeling tropical convergence based on the moist static energy budget. *Mon. Weather Rev.* **115**, 3–12 (1987).
41. Yan, Z. et al. Eastward shift and extension of ENSO-induced tropical precipitation anomalies under global warming. *Sci. Adv.* **6**, eaax4177 (2020).
42. Liu, Z. Y. et al. Evolution and forcing mechanisms of El Niño over the past 21,000 years. *Nature* **515**, 550–553 (2014).
43. Stevenson, S., Capotondi, A., Fasullo, J. & Otto-Bliesner, B. Forced changes to twentieth century ENSO diversity in a last Millennium context. *Clim. Dynam.* **52**, 7359–7374 (2019).
44. Zheng, X. T., Hui, C. & Yeh, S. W. Response of ENSO amplitude to global warming in CESM large ensemble: uncertainty due to internal variability. *Clim. Dynam.* **50**, 4019–4035 (2018).
45. Wang, L., Chen, W. & Huang, R. Interdecadal modulation of PDO on the impact of ENSO on the East Asian winter monsoon. *Geophys. Res. Lett.* **35**, L20702 (2008).
46. Maher, N., Matei, D., Milinski, S. & Marotzke, J. ENSO change in climate projections: forced response or internal variability? *Geophys. Res. Lett.* **45**, 11390–11398 (2018).
47. Seager, R., Kushnir, Y., Nakamura, J., Ting, M. & Naik, N. Northern Hemisphere winter snow anomalies: ENSO, NAO and the winter of 2009/10. *Geophys. Res. Lett.* **37**, L14703 (2010).
48. Hu, K., Xie, S.-P. & Huang, G. Orographically anchored El Niño effect on summer rainfall in central China. *J. Clim.* **30**, 10037–10045 (2017).
49. Chen, W., Feng, J. & Wu, R. Roles of ENSO and PDO in the link of the East Asian winter monsoon to the following summer monsoon. *J. Clim.* **26**, 622–635 (2013).
50. Seager, R., Naik, N. & Vogel, L. Does global warming cause intensified interannual hydroclimate variability? *J. Clim.* **25**, 3355–3372 (2012).

Methods

Datasets and index definition. We used the pre-industrial control runs and 1% yr^{-1} [CO_2] increase runs from 19 CGCMs of CMIP6. These were BCC-CSM2-MR, CESM2-WACCM, CESM2, CNRM-CM6-1, CNRM-ESM2-1, CanESM5, E3SM-1-0, EC-Earth3-Veg, GFDL-CM4, GFDL-ESM4, GISS-E2-1-G, GISS-E2-1-H, HadGEM3-GC31-LL, IPSL-CM6A-LR, MIROC-ES2L, MIROC6, MRI-ESM2-0, SAM0-UNICON and UKESM1-0-LL. To confirm the results, we performed two additional analyses. One was to analyse the changes from the historical scenario run (1950–1999) to the SSP585 run (2050–2099) in 30 CMIP6 models (Extended Data Fig. 3). The other was to analyse the changes from the historical scenario run (1950–1999) and the representative concentration pathway 8.5 run (2050–2099) in 18 CMIP5 models (Extended Data Fig. 2). The 30 CMIP6 models were ACCESS-CM2, ACCESS-ESM1-5, BCC-CSM2-MR, CESM2-WACCM, CESM2, CNRM-CM6-1-HR, CNRM-CM6-1, CNRM-ESM2-1, CanESM5-CanOE, GFDL-CM4, CanESM5, EC-Earth3-Veg, FGOALS-f3-L, FGOALS-g3, GFDL-CM4, GFDL-ESM4, GISS-E2-1-G, INM-CM4-8, INM-CM5-0, IPSL-CM6A-LR, KACE-1-0-G, MCM-UA-1-0, MIROC-ES2L, MIROC6, MPI-ESM1-2-HR, MPI-ESM1-2-LR, MRI-ESM2-0, NorESM2-LM, NorESM2-MM and UKESM1-0-LL. The 18 CMIP5 models were ACCESS1-0, BNU-ESM, CCSM4, CESM1-BGC, CNRM-CM5, CSIRO-Mk3-6-0, CanESM2, IPSL-CM5A-LR, IPSL-CM5A-MR, IPSL-CM5B-LR, MIROC-ESM-CHEM, MIROC-ESM, MIROC5, MRI-CGCM3, NorESM1-ME, NorESM1-M, bcc-csm1-1-m and bcc-csm1-1. More detailed online model documentations for the CMIP6 and CMIP5 models are available at https://pcmdi.llnl.gov/CMIP6/ and https://esgf-node.llnl.gov/search/cmip5/, respectively.

The MME is defined as the simple average of the 19 models. SST, precipitation, air temperature, geopotential height, winds, air specific humidity and vertical pressure velocity at 500 hPa were used. We constructed a DJF Niño3.4 SST index by averaging DJF SST anomalies in the domain of 5° S–5° N and 90°–150° W to indicate ENSO variations. ENSO-driven anomalies of specific humidity, air temperature, geopotential height, vertical pressure velocity and winds were calculated by regression on the DJF Niño3.4 SST index so that they represent variable anomalies per 1 K Niño3.4 SST index change. Before the regression analyses, the linear trend was removed. We also used a scaling method[36] to detrend the data and the result was almost the same as when applying a linear detrending method, indicating that the result is not sensitive to method choices (Extended Data Fig. 1).

For comparison, we calculated the observed ENSO-driven atmospheric anomalies based on the 2.5° latitude × 2.5° longitude daily National Centers for Environmental Prediction/Department of Energy version 2 Reanalysis[51] and Global Precipitation Climatology Project monthly precipitation datasets[52] and the 1° latitude × 1° longitude monthly Hadley Center SST[53] over 1979–2018. The results are shown in the Extended Data Figs. 4–6.

Moist static energy and moist instability analyses. MSE[40] is defined as $\mathrm{MSE} = C_p T + \phi + Lq$, where L is the latent heat of condensation, C_p is the specific heat capacity, T is the air temperature, ϕ is the geopotential and q is the air specific humidity. Thus, the change of ENSO-driven MSE anomalies ($\Delta\mathrm{MSE}'$) can be represented by $C_p\Delta T' + L\Delta q' + \Delta\phi'$. Here, $\Delta T'$, $\Delta q'$ and $\Delta\phi'$ denote the change of ENSO-driven anomalies of air temperature, specific humidity and geopotential, respectively. Since large-scale divergence tends to have a simple vertical structure in the tropics, with one sign in the lower troposphere and the opposite sign in the upper troposphere, for simplicity, we define gross moist instability (m) as the difference in moist static energy between the lower troposphere (1,000–500 hPa) and upper troposphere (500–200 hPa) following previous studies[13,37,40].

Statistical significance. We applied a 10,000-resampling bootstrap method to test whether the variance changes of the DJF Niño3.4 SST index, ENSO-related tropical-mean surface humidity and 200 hPa air temperature were statistically significant. For each of the three variables, its values in the 19 models were resampled randomly to construct 10,000 realizations of mean values. In this random resampling process, any model was allowed to be selected again. The 10,000 mean values were sorted in ascending order and the 250th and 9,750th values were set as the 2.5% lower confidence bound and the 97.5% upper confidence bound. Between the two bounds was the 95% confidence interval. In the observational analyses, the confidence level was based on a two-tailed Student's t-test.

Data availability

The CMIP6 data are available at https://pcmdi.llnl.gov/CMIP6/. The CMIP5 data are available at https://esgf-node.llnl.gov/search/cmip5/. The version 2 National Centers for Environmental Prediction/Department of Energy reanalysis and Global Precipitation Climatology Project precipitation data are from http://www.esrl.noaa.gov/psd/data/gridded/. Hadley Center SST data were provided by the Met Office Hadley Center (https://www.metoffice.gov.uk/hadobs/hadisst/).

Code availability

The code associated with this paper is available on request from K.H.

References

51. Kanamitsu, M. et al. NCEP-DOE AMIP-II reanalysis (R-2). *Bull. Am. Meteorol. Soc.* **83**, 1631–1643 (2002).
52. Adler, R. F. et al. The Version-2 Global Precipitation Climatology Project (GPCP) Monthly Precipitation Analysis (1979–present). *J. Hydrometeorol.* **4**, 1147–1167 (2003).
53. Rayner, N. A. et al. Global analyses of sea surface temperature, sea ice, and night marine air temperature since the late nineteenth century. *J. Gerophys. Res.* **108**, 4407 (2003).

Acknowledgements

The work was supported by the National Key Research and Development Program of China (fund number 2019YFA0606703), National Natural Science Foundation of China (41831175), Second Tibetan Plateau Scientific Expedition and Research (STEP) programme (grant number 2019QZKK0102), Strategic Priority Research Program of the Chinese Academy of Sciences (XDA20060500), National Natural Science Foundation of China (41775086, 41722504 and 91937302), Key Deployment Project of the Centre for Ocean Mega-Research of Science, Chinese Academy of Sciences (COMS2019Q03) and Youth Innovation Promotion Association of CAS. Y.K. was supported by the Japan Ministry of Education, Culture, Sports, Science and Technology (JPMXD0717935457) and Japan Society for the Promotion of Science (18H01278, 18H01281 and 19H05703). S.-P.X. was supported by the National Science Foundation (AGS 1934392).

Author contributions

K.H. and G.H. conceived the study, performed the analyses, built the mechanism and wrote the paper. P.H., Y.K. and S.-P.X. contributed to improving the paper and assisted in interpretation of the results.

Competing interests

The authors declare no competing interests.

Additional information

Extended data is available for this paper at https://doi.org/10.1038/s41561-021-00730-3.

Correspondence and requests for materials should be addressed to K.H. or G.H.

Peer review information Primary Handling Editor: Tom Richardson. *Nature Geoscience* thanks Tobias Bayr, Andrea Taschetto and the other, anonymous, reviewer(s) for their contribution to the peer review of this work.

Reprints and permissions information is available at www.nature.com/reprints.

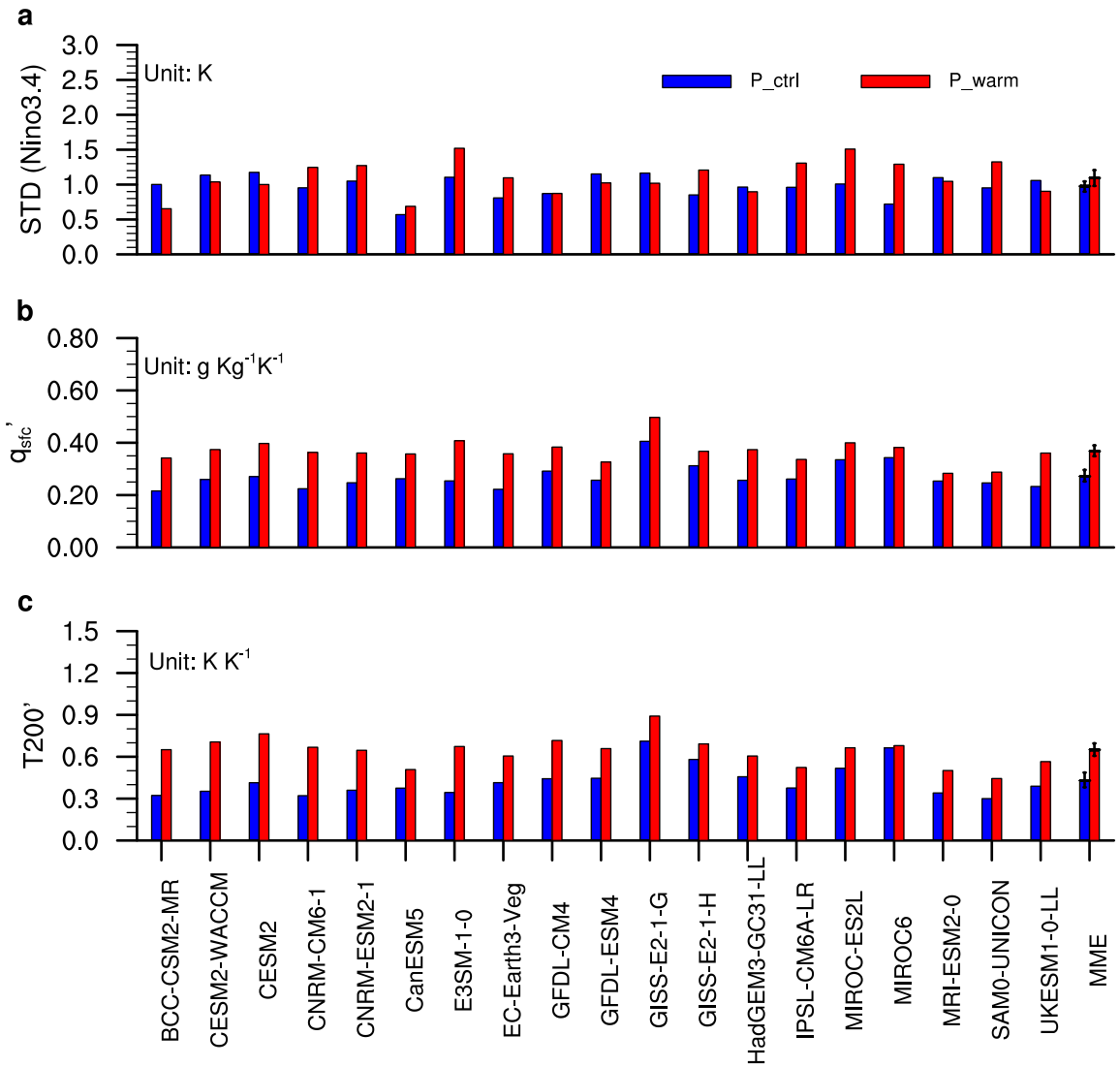

Extended Data Fig. 1 | Projected change in ENSO-driven variability in boreal winter tropical SST, humidity and air temperature. The analysis is the same as that in Fig. 1 except for applying a "scaling" method (see Method) for detrending data prior to regressions. The result is almost the same as that in Fig. 1, indicating the result is not sensitive to the selection of method for detrending.

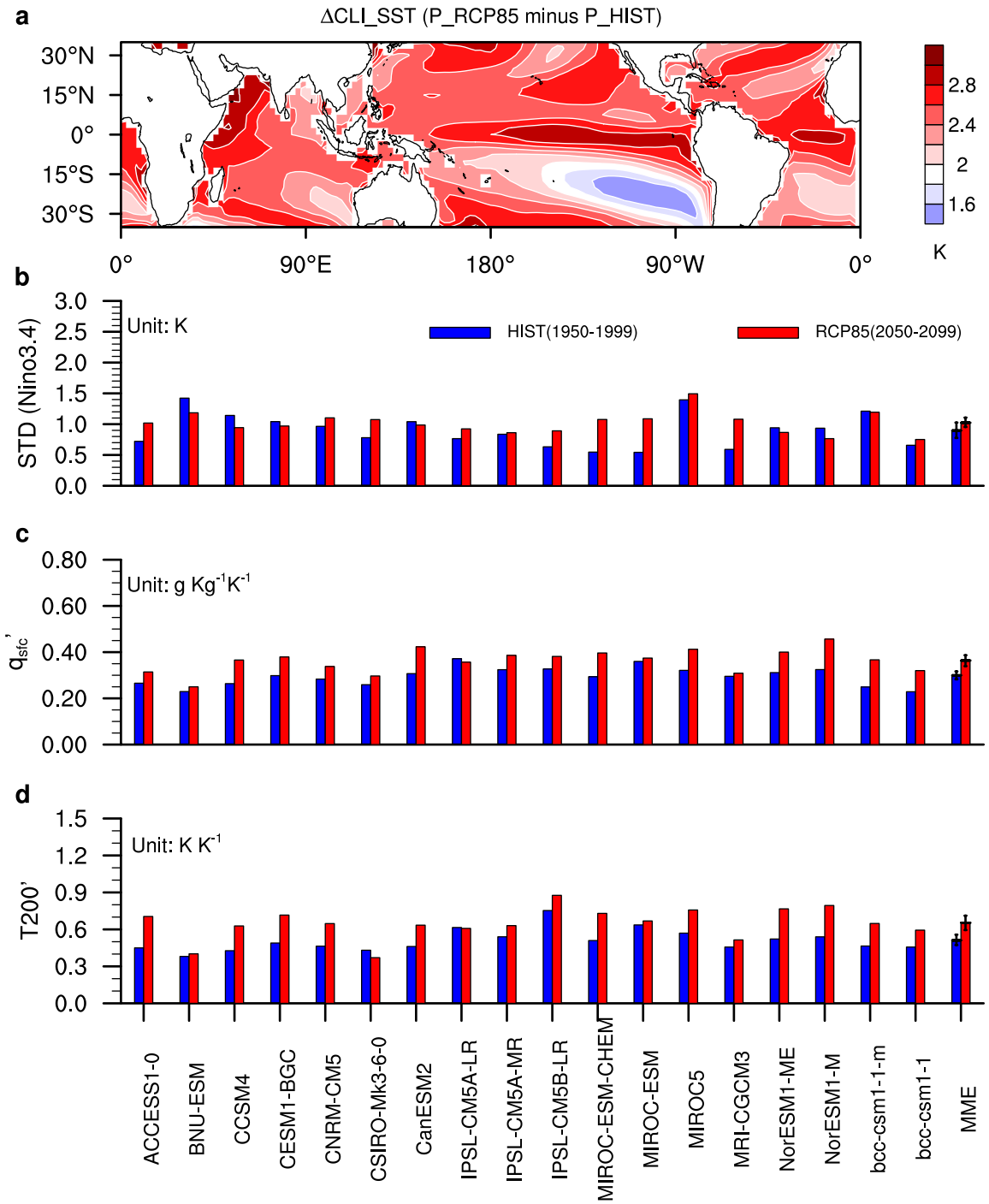

Extended Data Fig. 2 | Projected change in ENSO SST, humidity and air temperature in 18 CMIP5 models (see Methods) from 1950-1999 in historical experiments to 2050-2099 in RCP8.5 experiments. a, Changes in DJF climatological SST in the MME. **b**, Comparison of the standard deviation of DJF Niño 3.4 SST index over the two periods in each model and the MME. **c, d**, Comparison of DJF tropical mean (10°S-10°N) ENSO-driven surface specific humidity (q'_{sfc}; **c**) and 200-hPa air temperature (T'_{200}; **d**) between the two periods. Error bars in the MME mean correspond to the 95% confidence interval (see Methods). The MME q'_{sfc} and T'_{200} increases by 9.6±6.1% and 11.5±8.4% respectively for per 1K background warming in the tropics.

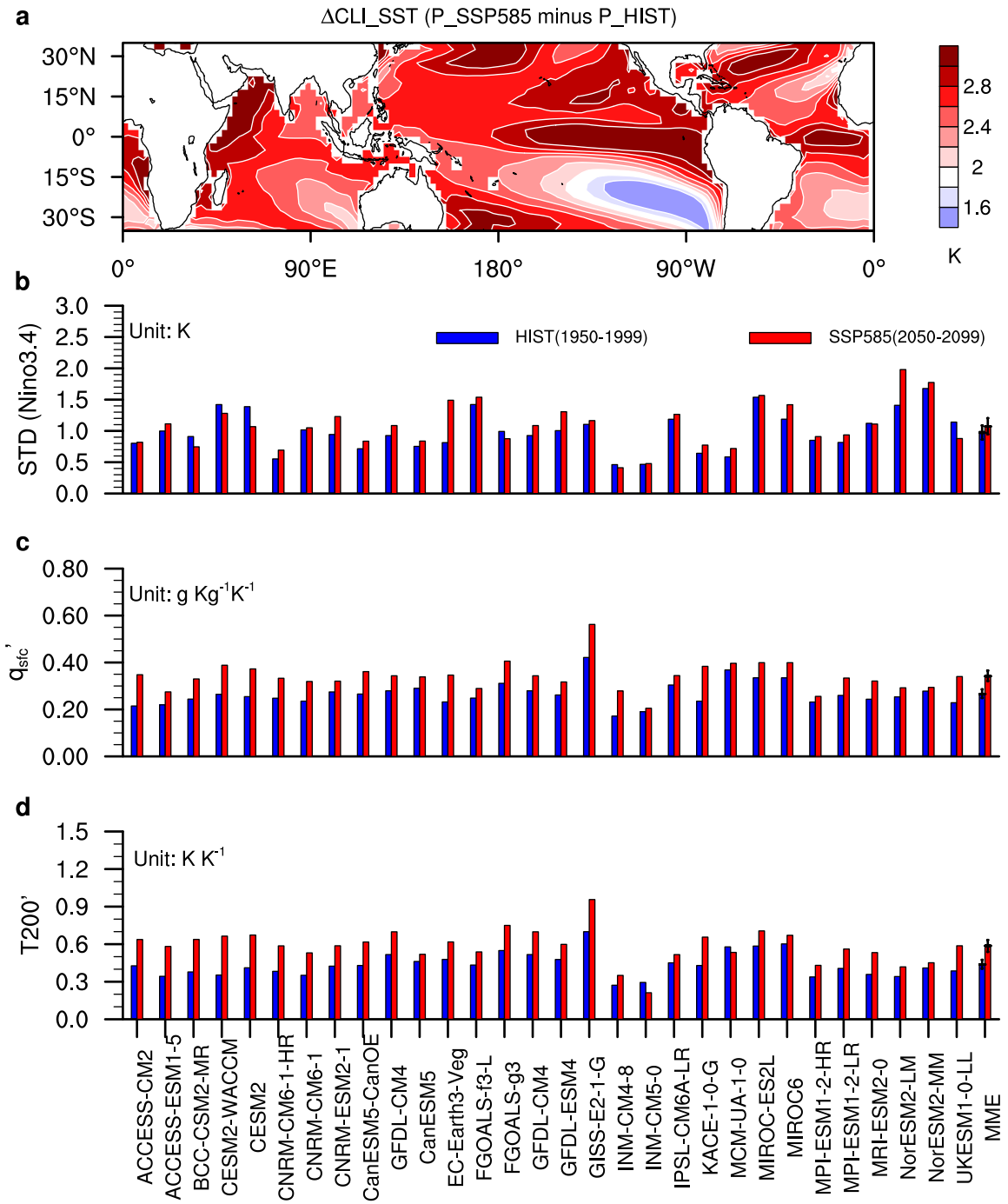

Extended Data Fig. 3 | Projected change in ENSO SST, humidity and air temperature in 30 CMIP6 models (see Methods) from 1950-1999 in historical experiments to 2050-2099 in SSP585 experiments. a, Changes in DJF climatological SST in the MME. **b**, Comparison of the standard deviation of DJF Niño 3.4 SST index over the two periods in each model and the MME. **c, d**, Comparison of DJF tropical mean (10°S-10°N) ENSO-driven surface specific humidity (q'_{sfc}; **c**) and 200-hPa air temperature (T'_{200}; **d**) between the two periods. Error bars in the MME mean correspond to the 95% confidence interval (see Methods). The MME q'_{sfc} and T'_{200} increases by 10.2±6.0% and 12.2±8.5% respectively for per 1K background warming in the tropics.

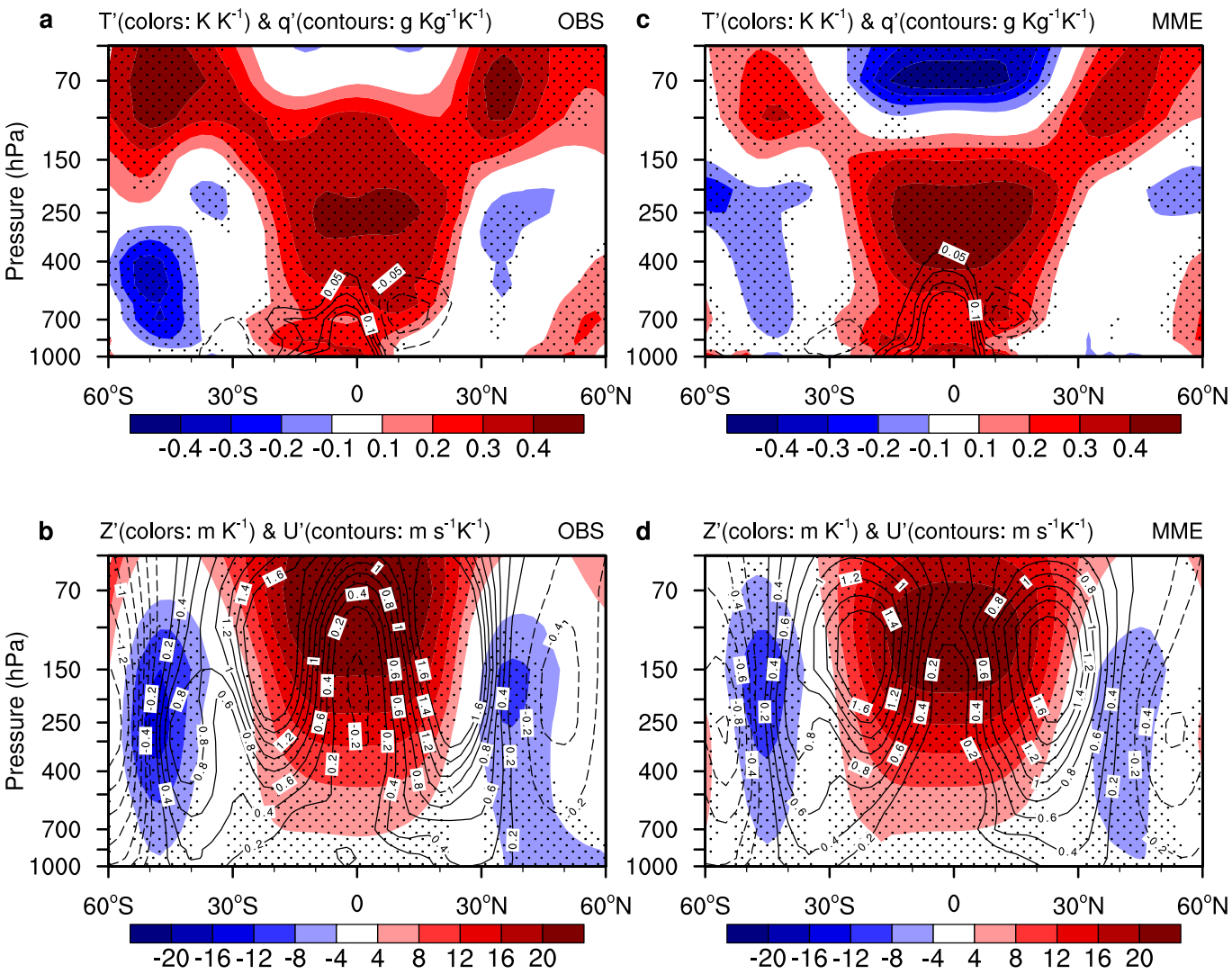

Extended Data Fig. 4 | Vertical structure of ENSO-driven anomalies of boreal winter air humidity, temperature and circulation. a, DJF zonally mean ENSO-driven specific humidity anomalies (q′; contours; at interval of 0.05 g kg^{-1} K^{-1}) and air temperature anomalies (T′; colors) during 1979-2018 in the observations. **b**, DJF zonally mean ENSO-driven zonal wind anomalies (U′; black contours; at interval of 0.2 m s^{-1} K^{-1}) and geopotential height anomalies (Z′; colors) during 1979-2018 in the observations. **c**-**d**, similar to **a** and **b** but for the MME during 400-449 model years in the PI control runs. Stippling in **a** and **b** denotes passing 95% confidence level based on a two-tailed Student's t test, and in **c** and **d** indicates that more than 85% of models agree on the sign of the MME.

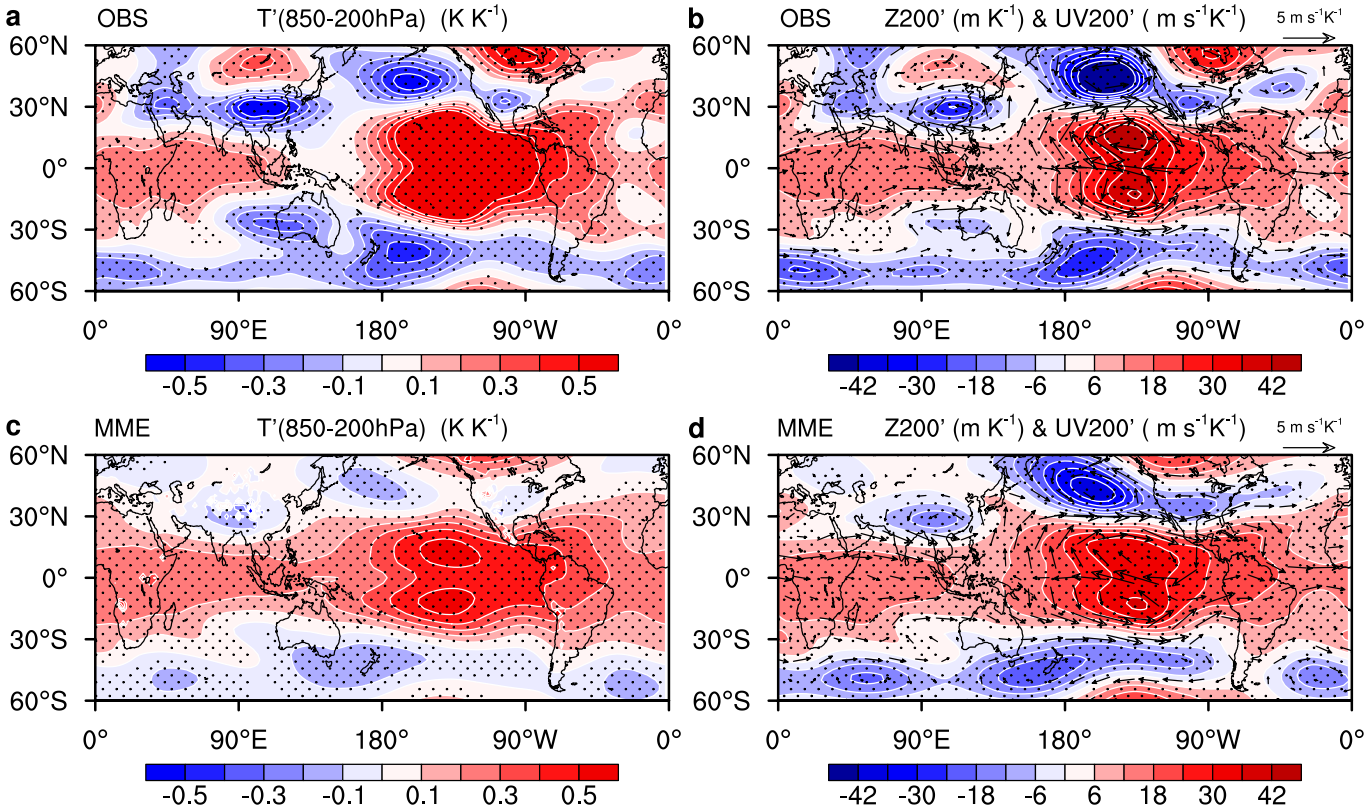

Extended Data Fig. 5 | ENSO-driven anomalies of boreal winter tropospheric air temperature, 200hPa geopotential height and circulation. a and **c**, Vertically averaged (850-200 hPa) ENSO-driven DJF air temperature anomalies (T′). **b** and **d**, 200-hPa ENSO-driven DJF geopotential height (Z200′; colors) and wind (UV200′; vectors) anomalies. Anomalies in **a** and **b** are derived from the observations during 1979-2018, while in **c** and **d** are from the MME during 400-449 model years in the PI control runs. Stippling in **a** and **b** denotes passing 95% confidence level based on a two-tailed Student's t test, and in **c** and **d** indicates that more than 85% of models agree on the sign of the MME.

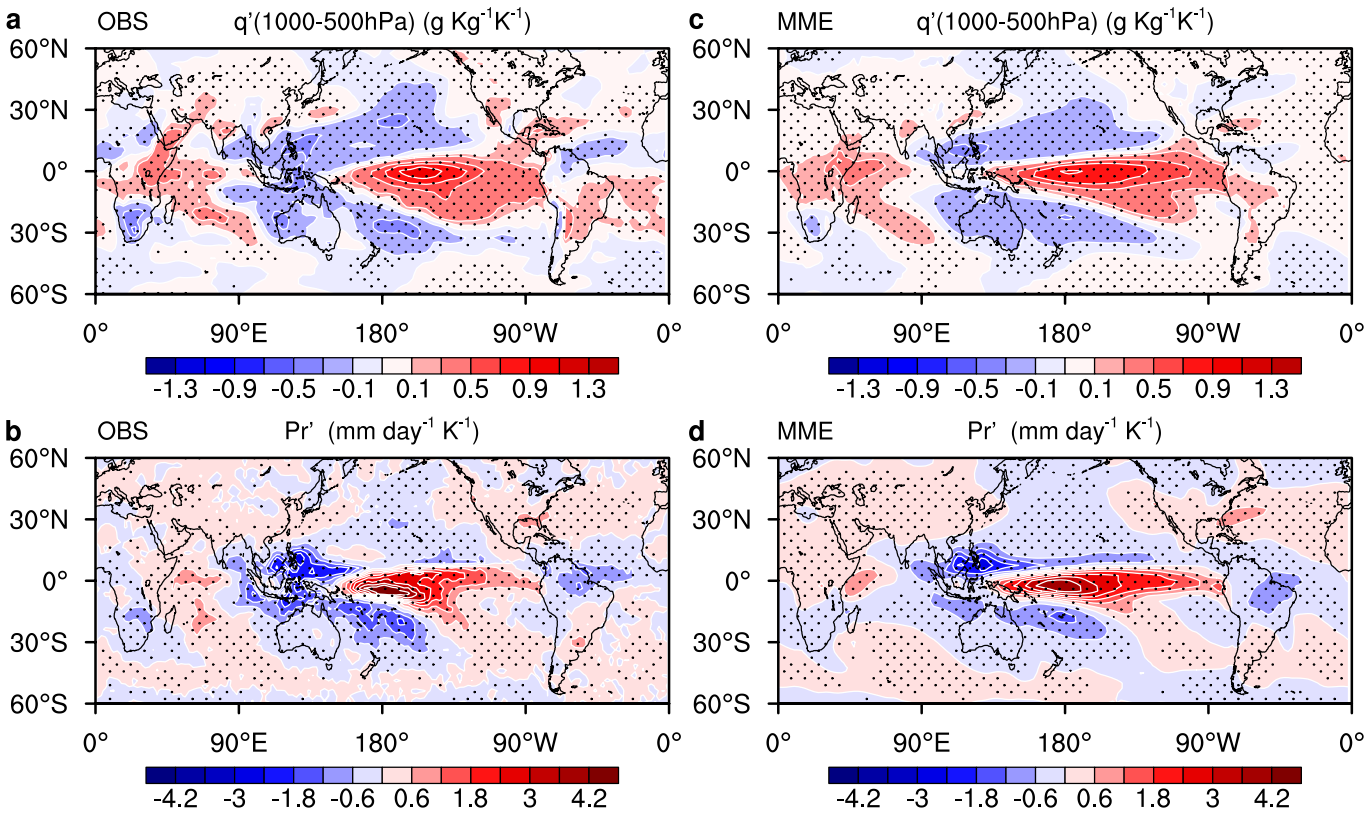

Extended Data Fig. 6 | ENSO-driven DJF anomalies in boreal winter specific humidity and rainfall. a and **c**, ENSO-driven DJF low-level 1000-500hPa vertically averaged specific humidity anomalies (q'). **b** and **d**, ENSO-driven DJF rainfall anomalies (Pr'). Anomalies in **a** and **b** are derived from the observations during 1979-2018, while in **c** and **d** are from the MME during 400-449 model years in the PI control runs. Stippling in **a** and **b** denotes passing 95% confidence level based on a two-tailed Student's t test, and in **c** and **d** indicates that more than 85% of models agree on the sign of the MME.

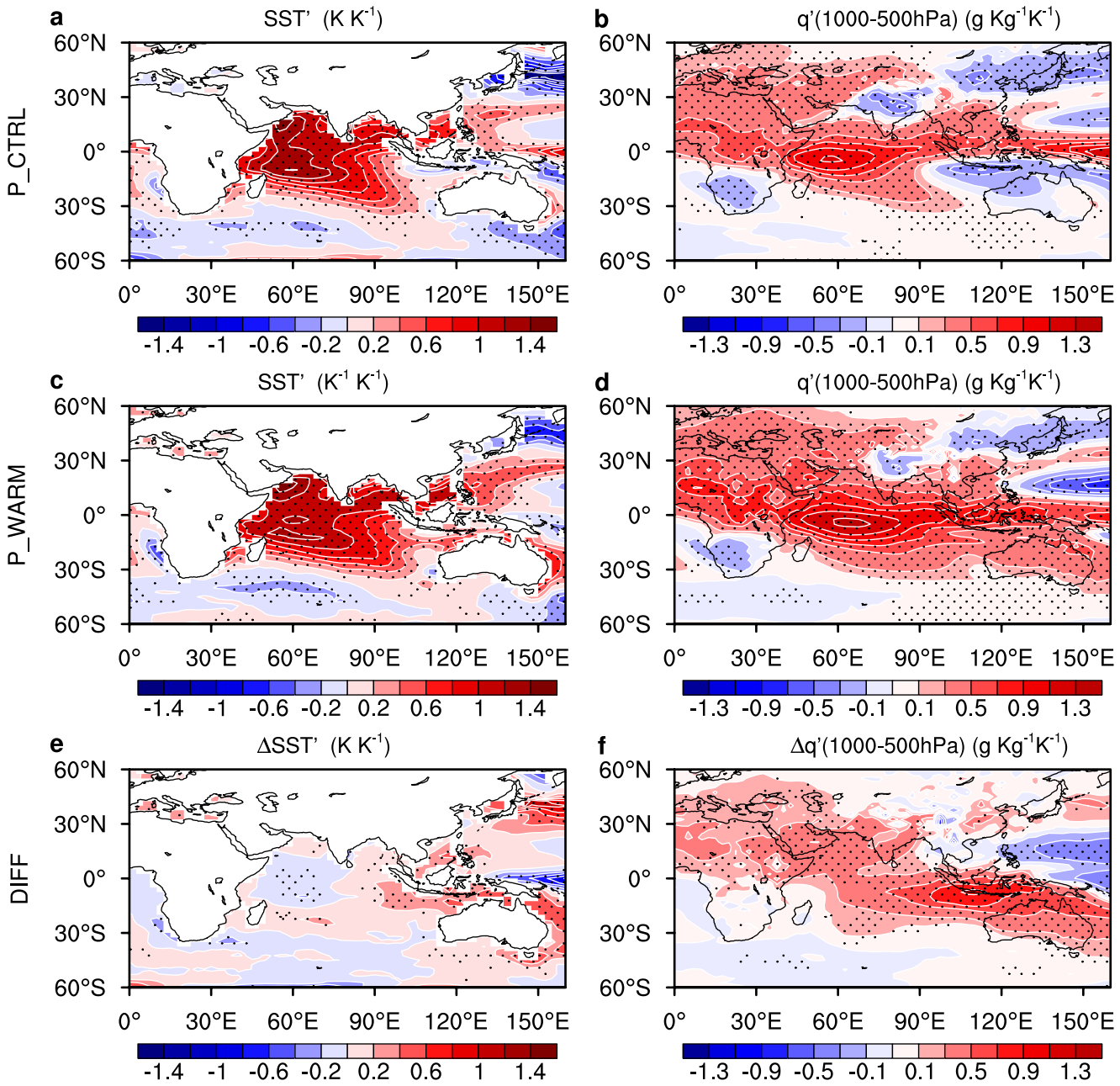

Extended Data Fig. 7 | Changes in the response of specific humidity to tropical Indian Ocean SST variability under global warming. a and **b**, The regression of June-to-August (JJA) mean SST **(a)** and 1000-500hPa vertically averaged specific humidity **(b)** onto a tropical Indian Ocean SST index in the period of P_ctrl. The tropical Indian Ocean SST index is defined as averaging JJA SST anomalies in the domain of 10°S-10°N, 40°E-100°E. **c** and **d**, Similar to **a** and **b** but for the period of P_warm. **e** and **f**, Differences between the two periods (P_warm- P_ctrl). Stippling indicates that more than 85% of models agree on the sign of the MME. The result shows that the response of specific humidity to tropical Indian Ocean SST variability strengthens under global warming.

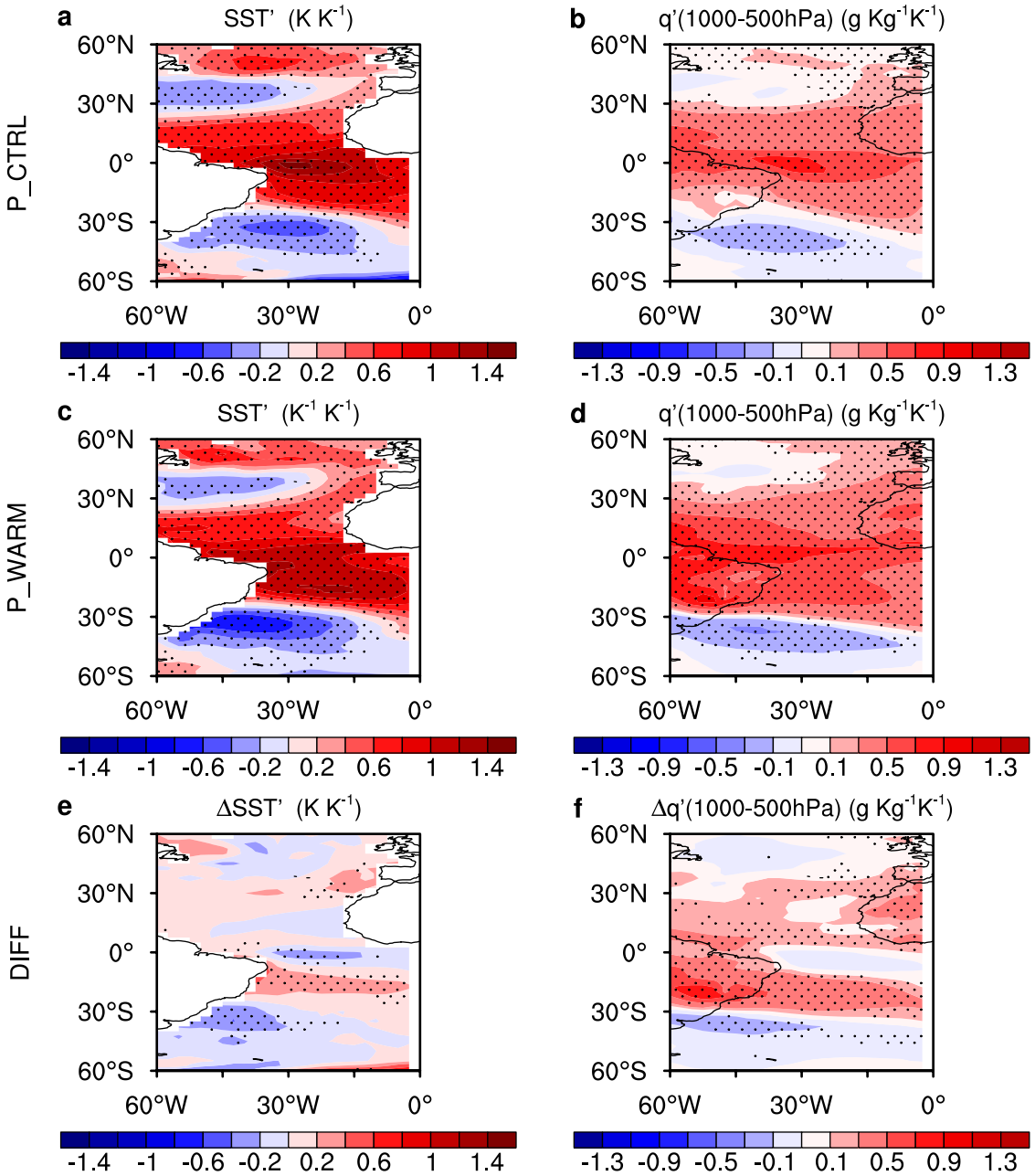

Extended Data Fig. 8 | Changes in the response of specific humidity to tropical Atlantic SST variability under global warming. a and **b**, The regression of JJA SST (**a**) and 1000-500hPa vertically averaged specific humidity (**b**) onto a tropical Atlantic SST index in the period of P_ctrl. The tropical Atlantic SST index is defined as averaging JJA SST anomalies in the domain of 10°S-10°N, 60°W-0°. **c** and **d**, Similar to **a** and **b** but for the period of P_warm. **c** and **d**, Differences between the two periods (P_warm- P_ctrl). Stippling indicates that more than 85% of models agree on the sign of the MME. The result shows that the response of specific humidity to tropical Atlantic SST variability strengthens under global warming.